The suppression of fluorescence peaks in energy-dispersive X-ray diffraction

Journal of
Applied Crystallography
ISSN 1600-5767

The suppression of fluorescence peaks in energy-dispersive X-ray diffraction

G. M. Hansford, S. M. R. Turner, D. Staab and D. Vernon

J. Appl. Cryst. (2014). **47**, 1708–1715

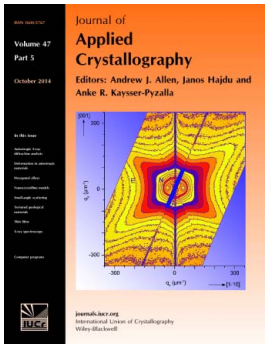

Journal of
Applied Crystallography
ISSN 1600-5767

Received 8 May 2014
Accepted 26 August 2014

The suppression of fluorescence peaks in energy-dispersive X-ray diffraction

G. M. Hansford,[a]* S. M. R. Turner,[a] D. Staab[b] and D. Vernon[a]

[a]University of Leicester, Space Research Centre, Department of Physics and Astronomy, Leicester LE1 7RH, UK, and [b]The Open University, Department of Physical Sciences, Walton Hall, Milton Keynes MK7 6AA, UK. Correspondence e-mail: gmh14@leicester.ac.uk

A novel method to separate diffraction and fluorescence peaks in energy-dispersive X-ray diffraction (EDXRD) is described. By tuning the excitation energy of an X-ray tube source to just below an elemental absorption edge, the corresponding fluorescence peaks of that element are completely suppressed in the resulting spectrum. Since *Bremsstrahlung* photons are present in the source spectrum up to the excitation energy, any diffraction peaks that lie at similar energies to the suppressed fluorescence peaks are uncovered. This technique is an alternative to the more usual method in EDXRD of altering the scattering angle in order to shift the energies of the diffraction peaks. However, in the back-reflection EDXRD technique [Hansford (2011). *J. Appl. Cryst.* **44**, 514–525] changing the scattering angle would lose the unique property of insensitivity to sample morphology and is therefore an unattractive option. The use of fluorescence suppression to reveal diffraction peaks is demonstrated experimentally by suppressing the Ca *K* fluorescence peaks in the back-reflection EDXRD spectra of several limestones and dolomites. Three substantial benefits are derived: uncovering of diffraction peak(s) that are otherwise obscured by fluorescence; suppression of the Ca *K* escape peaks; and an increase in the signal-to-background ratio. The improvement in the quality of the EDXRD spectrum allows the identification of a secondary mineral in the samples, where present. The results for a pressed-powder pellet of the geological standard JDo-1 (dolomite) show the presence of crystallite preferred orientation in this prepared sample. Preferred orientation is absent in several unprepared limestone and dolomite rock specimens, illustrating an advantage of the observation of rocks in their natural state enabled by back-reflection EDXRD.

1. Introduction

In the usual implementation of energy-dispersive X-ray diffraction (EDXRD), the sample is illuminated with white radiation and the diffracted radiation is recorded with an energy-dispersive solid state detector. Relative to the more conventional angle-dispersive XRD in which monochromatic radiation is used together with angle scanning of a detector, EDXRD presents several advantages and disadvantages, described, for example, by Laine & Lähteenmäki (1980) and Caminiti & Albertini (1999). The considerably poorer resolution of EDXRD limits its applicability as a general-purpose XRD method, but the advantages of fixed geometry and rapid and simultaneous data collection are crucial in certain applications. For the analysis of samples in extreme environmental conditions, such as high pressure and high or low temperatures, a static geometry is of great help in the experimental design; many examples can be found in the literature, such as Ma *et al.* (2001) and Higginbotham *et al.* (2014). The speed of EDXRD, especially when implemented at synchrotron facilities, allows dynamical analysis of materials such as the growth and phase transformations of crystals (Ellmer *et al.*, 2003; Caminiti & Albertini, 1999; Kellermeier *et al.*, 2013) and *operando* probing of the processes taking place in, for example, batteries (Kirshenbaum *et al.*, 2014). The advantages of speed and fixed geometry are combined in tomographic diffraction imaging methods (Scarlett *et al.*, 2009; Cernik *et al.*, 2008; Harding, 2009), which generally use high-energy X-rays at low scattering angles to probe volumes that are otherwise obscured. The simplicity of EDXRD can be advantageous in the design of portable instruments used in the analysis of heritage objects (Uda, 2004; Uda *et al.*, 2005; Cuevas & Gravie, 2011) and in security applications (Peterzol *et al.*, 2011).

A disadvantage of EDXRD is the potential for overlap of X-ray fluorescence (XRF) peaks and diffraction peaks (Laine & Lähteenmäki, 1980; Voskamp, 1974). The usual method to separate the two, if it is necessary to do so, is to alter the scattering angle so that the diffraction peaks shift to different energies while the fluorescence peaks, of course, remain static

(Sparks & Gedcke, 1972; Voskamp, 1974; Sutton *et al.*, 1986). This method also serves to unambiguously distinguish fluorescence and diffraction peaks.

In this paper, a novel method to separate fluorescence and diffraction peaks is described. This technique involves the suppression of fluorescence peaks in order to uncover any diffraction peaks that are otherwise obscured, noting that XRF normally gives rise to much more intense peaks unless the fluorescing element is present only in trace quantities. The method was conceived in connection with the back-reflection EDXRD technique (Hansford, 2011*a*, 2013). This technique is uniquely insensitive to sample morphology and can be applied to specimens with no or very little sample preparation. This characteristic, together with the speed of EDXRD and the back-reflection geometry, are highly suited to the design and development of a handheld instrument. A key limitation is the low resolution of diffraction peaks relative to laboratory-based XRD, but the method is expected to be sufficiently good for applications such as mining and analysis of cultural heritage objects where the number of minerals present is relatively small and some information regarding their identities is likely to be available in advance. The aim in applications of this type is mineral identification and approximate quantification. Low instrument mass combined with the lack of a sample preparation requirement are also highly beneficial characteristics for the development of a space instrument for planetary exploration. Back-reflection EDXRD is a powder diffraction method and is therefore not suited to (unprepared) samples with large crystallites, which would give unrepresentative diffraction peak intensities. It is worth noting that the resolution of back-reflection EDXRD is limited by the solid state detector, if one is used to provide the energy-dispersing capability. There is no fundamental resolution limit imposed by the technique itself, and implementation of a high-resolution version is perfectly feasible at, for example, synchrotron facilities.

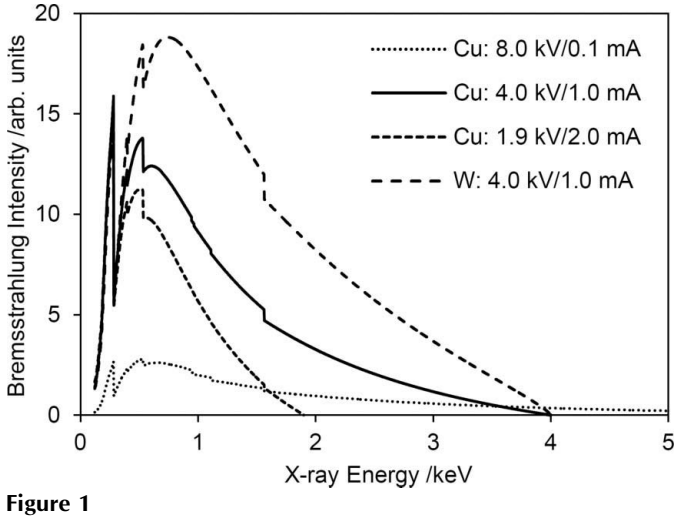

Figure 1
Calculated X-ray tube *Bremsstrahlung* output, after transmission through the optical filter, at several different excitation voltages/emission currents: 8.0 kV/0.1 mA, 4.0 kV/1.0 mA and 1.9 kV/2.0 mA for a Cu anode, and 4 kV/1.0 mA for a W anode. Characteristic lines (Cu *L* and W *M* series) were not included in the calculation. The vertical axis is in arbitrary units, but proportional to photons s^{-1} sr^{-1}. The horizontal axis is shown up to 5 keV for ease of comparison with Fig. 3.

The application of EDXRD in the back-reflection geometry shifts diffraction peaks to their lowest possible energies, and consequently the potential for overlap with fluorescence peaks is greatest, especially for geological samples (Hansford, 2011*a*). The fluorescence suppression technique described in this paper is therefore particularly suitable for back-reflection EDXRD, but it is emphasized that it can be applied to EDXRD at any scattering angle. It has the advantage of avoiding the need to change the instrument geometry or to have an additional detector mounted at a second scattering angle.

The principle of the fluorescence suppression method is described in §2, and the experimental method employed to demonstrate the technique is given in §3. A ray-tracing model is used to help interpret the results, and this model is described in §4. The results of the experiments with several limestone and dolomite samples are presented in §5, followed by discussion and conclusions in §6.

2. Suppression of fluorescence peaks

In laboratory-based EDXRD, a continuum of X-ray energies is commonly produced using an X-ray tube source. The upper energy limit of the continuum is controlled by the excitation voltage of the source and can be tuned to a desired value with the control electronics. Sample XRF peaks can be selectively suppressed, without eliminating diffraction peaks lying at the same or very similar energies, by taking advantage of the difference between the characteristic XRF energies and the corresponding absorption edge. For example, the Ca *K* absorption edge lies at 4.034 keV, while the $K\alpha$ and $K\beta$ lines are at 3.691 and 4.013 keV, respectively (Kaye & Laby, 2005) ($K\alpha$ energies are quoted as the intensity-weighted average of the $K\alpha_1$ and $K\alpha_2$ components in this paper). If the excitation voltage is tuned to just below the absorption edge energy, for example 4.03 keV, there will be X-ray photons in the beam incident on the sample up to this energy available for diffraction, while Ca *K* fluorescence is guaranteed to be completely absent. Experimental data that prove this principle are presented in §5.

The calculated (Ebel, 1999) X-ray intensity *versus* energy for the *Bremsstrahlung* output of an X-ray tube is shown in Fig. 1 at several different excitation voltages and emission currents. Looking at the output with a Cu anode at 4.0 kV, this plot makes clear a limitation of the described fluorescence suppression technique – the output intensity is very low as the energy approaches the upper limit and diffraction peaks in this energy region will be correspondingly weak. There are several ways to mitigate this limitation. Firstly, the emission current of the tube source can be increased to give a proportional increase in X-ray output. Secondly, a high atomic number element can be used for the anode. Fig. 1 compares the output of Cu (Z = 29) and W (Z = 74) anodes; the enhancement in intensity from the latter over the former is quite substantial. A third possibility is to set the excitation voltage to slightly

above the absorption edge energy, for example 4.1 keV for the Ca *K* edge. Although the source will emit some X-rays above the absorption edge, the flux will be very low and the fluorescence peaks will be correspondingly weak. This method may be effective for minor sample elements which nevertheless would otherwise have sufficiently strong fluorescence peaks to obscure diffraction signals.

The suppression of fluorescence peaks by tuning of the tube excitation voltage can, in principle, be applied to any fluorescence peak produced by any element. It is expected to be decreasingly effective towards lower energies because the separation of the characteristic fluorescence energies and the corresponding absorption edge is smaller. For example, Si $K\alpha$ lies at 1.740 keV, while the Si *K* edge is at 1.840 keV, a difference of only 100 eV compared with 343 eV for Ca *K*. Together with the intensity factor described in the preceding paragraph, quite a small energy range is effectively 'uncovered' by the suppression technique for Si *K*. The method can also be applied to *L*-series (and *M*-series *etc.*) fluorescence, with the added complexity of three sub-shells, each with its own absorption edge.

3. Experimental method

The fluorescence suppression technique has been demonstrated for EDXRD in the back-reflection geometry. Experimental data were acquired using the setup described in more detail by Hansford (2013). This setup consists of an in-house designed and built X-ray tube source with a copper anode, an aperture to restrict the width of the X-ray beam, a sample holder and an e2v CCD-22 imaging detector, all contained within a vacuum chamber. The sample holder is mounted on a rotation stage which allows the incident angle of the X-ray beam to be altered. The silicon-based CCD sits on a rotary arm such that the source–sample–detector angle (*i.e.* the 2θ scattering angle) can be chosen within the range of approximately 80–170°. The CCD is cooled using a liquid-nitrogen bath and was operated at 183 K for the results presented here. A full width at half-maximum spectral resolution of 195 eV was achieved at an X-ray energy of 5.9 keV. To prevent light from the X-ray tube filament electron source reaching the light-sensitive detector, a light baffle and an optical filter are positioned between the X-ray tube and the main chamber of the experiment. The only change to the configuration described in the earlier paper was that the 15 µm Al optical filter was replaced with a much thinner one consisting of a 2 µm polyimide film with a 1 µm Al coating. The quoted layer thicknesses are nominal and have not been confirmed experimentally. This change was made in order to achieve a much higher throughput of X-ray intensity, as illustrated in Fig. 2 of Hansford (2013). Except where noted otherwise, data sets were acquired over a period of three hours and data from only the top third of the imaging area of the CCD were used to derive the X-ray spectra presented here. The CCD was operated in photon-counting mode in order to achieve good spectral resolution (Burrows *et al.*, 2005). At higher excitation voltages, for example 4 kV and above, the emission current must be limited to a value that avoids significant pile-up. The maximum emission current that can be achieved in the existing setup is 2.0 mA, and this current was used at lower excitation voltages such as 1.9 kV.

Several different hand specimens of rocks and a pressed-powder pellet were mounted in the vacuum chamber during the course of the experiments. The hand specimens were attached to a sample mount as described previously, using copper wire, while the pellet was mounted in a purpose-built holder.

The fluorescence suppression method requires that the X-ray tube excitation voltage can be set with an accuracy of the order of ±0.05 keV or better. In the current setup, this voltage is set with the aid of an analogue meter with marked intervals of 0.2 keV, which is not as fine as desirable. In practice, there is a degree of trial and error in the setting of the excitation voltage, with the presence or absence of the suppression-targeted fluorescence peaks being used to establish the correct setting. The reproducibility of the setting has been found to be good.

4. Model description

A simulation program, *PoDFluX* (Hansford, 2009), was used as an aid in the interpretation of the results. This program is a Monte Carlo ray-tracing model that simulates X-ray diffraction and fluorescence from a sample onto an imaging and energy-resolving detector. The source can be specified as an X-ray tube, ^{55}Fe radioisotope or synchrotron-like source (the beam characteristics are defined rather than explicit simulation of beam insertion devices). The program has been used to optimize instrumental parameters such as geometry (Hansford, 2011*b*, 2012) and to investigate novel XRD geometries (Hansford, 2011*a*). Since this program was first reported, several improvements and extensions have been made, and the most significant of these are summarized here.

Whereas in the original implementation of *PoDFluX* the effect of X-ray penetration into the sample on diffraction and fluorescence intensities was accounted for, the geometric effect was not, *i.e.* the interactions took place exactly on the sample surface. Penetration depths into the sample are now calculated using a probability distribution function based on the Beer–Lambert law for attenuation of X-rays, and rays are traced to their calculated depths. *PoDFluX* can also now handle diffraction and fluorescence in transmission geometry. The model implicitly assumes a completely homogeneous sample – no account is taken of grain effects such as micro-absorption.

Several additional X-ray optics and components are now included in the model, namely beam stops, Soller slits (parallel, diverging or converging), and diffraction from mosaic crystals (Sánchez del Río *et al.*, 1992) and perfect crystals (Sánchez del Río & Cerrina, 1992), including asymmetrically cut crystals and symmetrically cut as a special case. The calculation of *L*-line intensities from an X-ray tube has been updated according to Ebel (2003).

Preferred orientation of crystallites in the sample can now be included in model simulations, in both symmetric and asymmetric diffraction geometries. The March–Dollase function (Dollase, 1986) is assumed for the density function of the preferentially oriented pole, but other functions could readily be substituted. Implementation for symmetric geometries is straightforward since it only involves a closed-formula modification to the diffraction intensities. Implementation for asymmetric geometries is significantly more complex because the effect on diffraction intensity is dependent on the position of the diffracted ray on the Debye–Scherrer ring. The method of implementation is based on a formulation proposed by Černý *et al.* (1995). Subject to certain conditions, the distribution of the poles of any plane (*hkl*) is given by equation (1) of Černý *et al.* (1995) (hereafter referred to as the Černý function). A conceptual framework is required in order to use the Černý function within a ray-tracing model; one is conveniently provided by the model developed by Sánchez del Río *et al.* (1992) for the ray tracing of diffraction from mosaic crystals. The Gaussian distribution of crystallite normals which was assumed for mosaic crystals is replaced by the Černý function for preferred orientation. Some additional complexity in the coding is introduced because the closed-formula Gaussian is replaced with a function that requires numerical evaluation of an integral. The latter is performed in *PoDFluX* using Romberg integration (Press *et al.*, 2007). A further complication is that sampling of the Černý distribution function must use the rejection method (Press *et al.*, 2007) rather than an inversion algorithm as described by Sánchez del Río *et al.* (1992).

For the simulations presented in this paper only the top third of the detector imaging area is included, reproducing the way in which the experimental data are processed. The model assumes an ideal powder sample with crystallites sufficiently small to produce smooth diffraction rings but not so small that peak broadening is induced. Apart from the simulations that include the effects of preferred orientation, completely random crystallite orientations are assumed. The model uses a smooth flat sample surface irrespective of whether the real sample is a pressed-powder pellet or a rock hand specimen with surface relief. Fortunately, in back-reflection EDXRD the difference is immaterial as long as the sample position in the model approximates the average position of the area of the real sample illuminated by the X-ray beam.

5. Results

The efficacy of the fluorescence suppression technique has been demonstrated using the same limestone hand specimen for which data were reported by Hansford (2013). The X-ray spectrum was reacquired under the same conditions as previously reported, except that the emission current was reduced from 0.4 to 0.1 mA because of the greater throughput of the optical filter. The Ca *K* fluorescence intensity in the new data set is 5% greater than that in the older data set. Fig. 2 shows the updated spectrum compared to the earlier one, and demonstrates a considerable improvement in the signal-to-background ratio for most of the peaks in the energy range up to ∼3.5 keV, as well as the appearance of diffraction peaks not previously observed. As before, the Ca *K* fluorescence peaks dominate the spectrum – the Ca *Kα* peak height is a factor of 62 greater than the height of the most intense diffraction peak at 2.01 keV. The vertical scale of this plot, and all the subsequent plots, has been chosen to highlight the diffraction peaks. The fluorescence peaks for the light elements up to Si are enhanced relative to Ca *K* fluorescence partly because fluorescence is more efficiently stimulated by X-rays relatively close in energy to the corresponding absorption edge energies (Potts, 1992).

The Ca *K* fluorescence peaks clearly dominate the spectra in Fig. 2 and are the obvious target for suppression. A new data set was acquired with the X-ray tube excitation voltage set to approximately 4.0 keV (within experimental uncertainty), just below the Ca *K* absorption edge at 4.034 keV, and an emission current of 1.0 mA. The resulting spectrum (Fig. 3) shows the complete suppression of Ca *K* fluorescence and concomitantly the uncovering of a weak peak at 3.87 keV, which is shown below to be a calcite, $CaCO_3$, diffraction peak. This spectrum is therefore a proof of the principle of the fluorescence suppression technique used to uncover diffraction peaks. Two additional benefits are also illustrated by this spectrum: the Ca *K* escape peaks (Bautz *et al.*, 1999) at 1.95 and 2.27 keV are also suppressed, and the background across the entire energy range up to the Ca *K* energies is significantly reduced, enhancing the peak-to-background ratios. The increased background in the 8 kV spectrum arises from charge-loss events in the CCD associated with Ca *K* fluorescence (Prigozhin *et al.*, 2000).

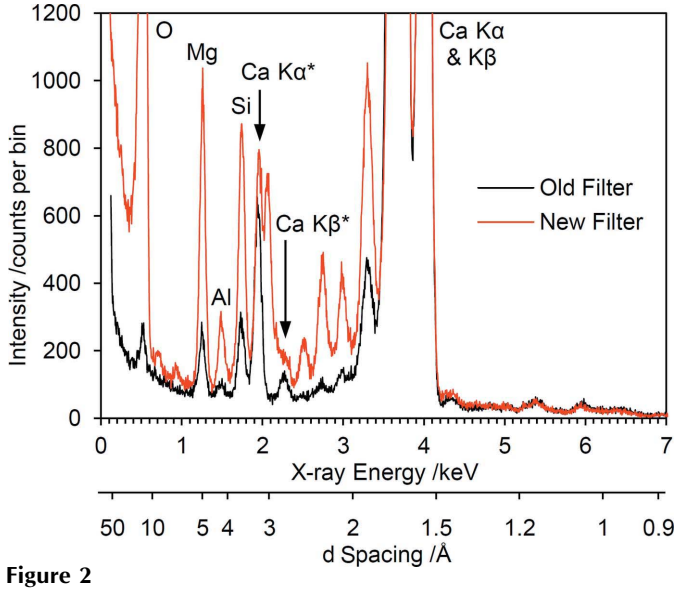

Figure 2
Back-reflection spectra of limestone A with the two different optical filters (see text for details). The excitation voltage is 8.0 kV in each case, and the emission currents are 0.4 mA for the 'old' filter and 0.1 mA for the 'new' filter. The fluorescence peaks are labelled, escape peaks with an asterisk; the unlabelled peaks are due to diffraction, including the weak features above 4 keV.

Fig. 3 also shows a spectrum in which Si *K* fluorescence has been suppressed. In this case, the tube excitation voltage was set to 1.9 kV (with an emission current of 2.0 mA), slightly above the Si *K* absorption edge. Consequently, there is a residual Si *K* fluorescence peak, though weaker than the adjacent calcite diffraction peak at 1.64 keV. The use of an excitation voltage above the absorption edge in this case is feasible because Si is present as a minor element only. Simulations suggest that if Si is present in the form of quartz (SiO_2), as is likely for a limestone, this mineral constitutes only 2.7% by volume of the sample, but it should be stressed that quartz has not been identified using these data. In contrast to Ca *K* suppression, quite limited additional spectral information is uncovered, as expected for lower-energy fluorescence.

The excitation voltages and emission currents used to generate the spectra shown in Fig. 3 match the values used for the calculation of the *Bremsstrahlung* output from the X-ray tube in Fig. 1. Comparing the 8.0 kV/0.1 mA setting with 4.0 kV/1.0 mA, the latter shows greater intensity below the cross-over point at ∼3.6 keV, and indeed the diffraction peaks in Fig. 3, where they can be compared, are stronger for the 4.0 kV/1.0 mA setting (the 8.0 kV data have been scaled by a relative factor of 2.5). Suppression of Ca *K* fluorescence at 4.0 kV excitation allowed a higher emission current to be used while still operating the CCD in photon-counting mode, and this illustrates a further advantage of the fluorescence suppression method.

Fig. 4 compares the Ca *K* suppressed data set with simulations for several different mineral combinations using the *PoDFluX* ray-tracing model. The main diffraction peaks are explained by calcite, as previously concluded (Hansford, 2013). The earlier paper speculated that the presence of Mg in the sample suggested the presence of dolomite, $CaMg(CO_3)_2$. This can now be confirmed with a high degree of confidence by comparison of the experimental spectrum with the simulation of 80% calcite/20% dolomite (volume %) – the two shoulders indicated in Fig. 4 are consistent with dolomite. Equally, the presence of magnesite, $MgCO_3$, can be excluded, except possibly as a trace component. Careful comparison of simulations with the experimental data suggest that calcite and dolomite are present in the ratio $(86 \pm 2):(14 \pm 2)$, though this quantification comes with two caveats. Firstly, the volume of the sample probed extends to a depth of only a few micrometres (Hansford, 2011*a*) and therefore is not necessarily representative of the whole rock composition. No tests have been performed to establish the degree of inhomogeneity of the specimen composition; visually, there is evidence of inhomogeneity at the centimetre scale. Secondly, *PoDFluX* calculates the diffraction peak intensities using a fundamental parameters approach, and the calculation is therefore limited by the accuracy of these parameters. Although *PoDFluX* has been validated for a variety of experimental geometries (Hansford, 2009), the quantification of different phases in a sample has not been confirmed by comparison with conventional XRD or other analytical techniques. Conversely, calcite and dolomite have closely related crystal structures and the calculation of the diffraction intensities relative to each other is likely to be significantly more reliable than the calculation of the absolute intensities.

Subsequent to the above analysis, a portion of this limestone sample was ground to a powder and analysed with a Bruker D8 Advance diffractometer. The resulting diffractogram is shown in Fig. 5 over the same *d*-spacing range as the data in Fig. 4. The ratio of minerals was not quantified, but it is

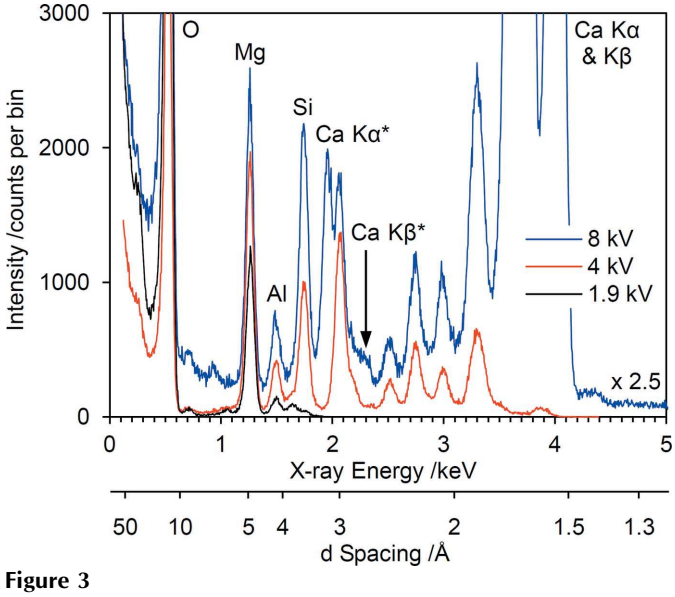

Figure 3
Back-reflection spectra of limestone A at three different excitation voltages/emission currents: 8.0 kV/0.1 mA, 4.0 kV/1.0 mA for Ca *K* suppression, and 1.9 kV/2.0 mA for Si *K* suppression (*cf.* Fig. 1). The 8.0 kV data have been multiplied by 2.5 to allow easier comparison. The Si *K* suppression data are taken from the whole imaging area of the CCD rather than the top third only because of the relatively low intensity.

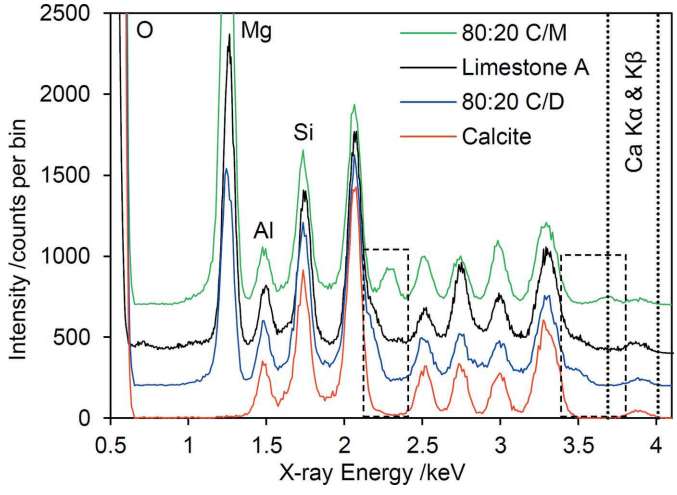

Figure 4
The Ca *K* suppressed back-reflection spectrum of limestone A alongside three simulations: calcite only, 80:20 calcite/dolomite (C/D) and 80:20 calcite/magnesite (C/M). The dotted lines indicate the energies of the suppressed Ca *K* fluorescence peaks, while the dashed boxes show the parts of the spectrum that allow the identification of dolomite and exclusion of magnesite. The sample compositions for the simulations include minor quartz and Al_2O_3 in order to reproduce the experimental Si and Al fluorescence peaks.

clear from the data that calcite dominates the sample composition, followed by dolomite. In addition, there are two weak peaks that are assigned to quartz. Thus, these results support the interpretation based on the energy-dispersive XRD data alone.

In order to establish whether the above limestone analysis is generally applicable to other limestones/dolomites, some additional samples were tested. Four of these samples are hand specimens of rocks, and one is a pressed-powder pellet of the Japanese geological standard JDo-1 (Imai *et al.*, 1996). Samples B–E are loose rocks which were picked up from the ground by two of the authors (GMH and DS), neither of whom has any geological training. The geology of each locality was known in advance, and it was anticipated that these samples were in all probability limestones or dolomites. Images of all of the hand specimens are shown in Fig. 6. Each of these samples was mounted in the vacuum chamber after, at most, light brushing of the surface to remove any loose material. It was clear from the analysis of sample A that the Ca *K* suppressed spectrum gives by far the most useful information for this type of geological sample. The corresponding spectra were acquired for each sample and are shown in Fig. 7. It is immediately clear (and the plot has been arranged to emphasize this point) that three of the samples are calcite dominated and three are dolomite dominated. Furthermore, it is possible to conclude with high confidence that four of the six samples (B–E) are essentially monomineralic. The JDo-1 sample is estimated to contain approximately 10% calcite, giving rise to a small shoulder on the strong diffraction peak at 2.17 keV and slightly enhanced intensity at the strong calcite diffraction peak at 3.29 keV. The authors are unaware of a published mineralogical analysis of the JDo-1 standard, but the XRD pattern shown on the Geological Survey of Japan web site (see https://gbank.gsj.jp/geostandards/gsj1maine.html) shows calcite peaks in addition to dolomite. The variable Al and Si fluorescence peaks in these spectra suggest variable amounts of minor Al- and Si-containing constituents.

The JDo-1 spectrum has an anomalously strong 104 diffraction peak, relative to samples D and E and to the model simulation. The enhanced strength of this peak can be attributed to preferred orientation of crystallites in the pellet sample. Both calcite and dolomite exhibit perfect cleavage along the (104) plane, and preferred orientation of this plane parallel to the powder surface, especially if pressed, is well known (Perdikatsis, 2000; Suzuki *et al.*, 1998). Preferred orientation of this plane was confirmed experimentally by tilting the JDo-1 sample about an axis perpendicular to the incident X-ray beam (Fig. 8). The effect on the strength of the 104 reflection is marked, while the difference is simultaneously minor or negligible for the other diffraction peaks in the spectrum. The simulations also shown in Fig. 8 reproduce this behaviour very well. The model assumes the March–Dollase description of preferred orientation (Dollase, 1986), and the best match with experiment is achieved with a March coefficient of $r = 0.53 \pm 0.03$. It should be noted that the diffraction geometry is not symmetric with respect to the diffraction vector, even when the sample is not tilted.

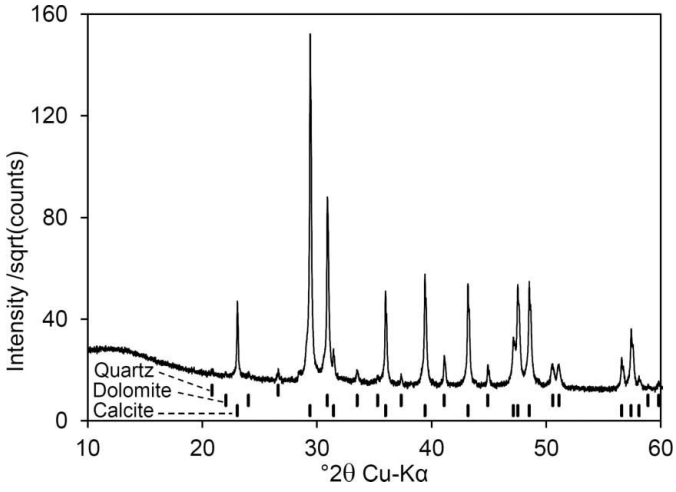

Figure 5
D8 Advance diffractogram of limestone A up to 60° in 2θ (Cu $K\alpha$). The assignment of peaks to calcite, dolomite and quartz is shown below the trace. Diffraction peaks that are predicted but are too weak to be observed are not indicated.

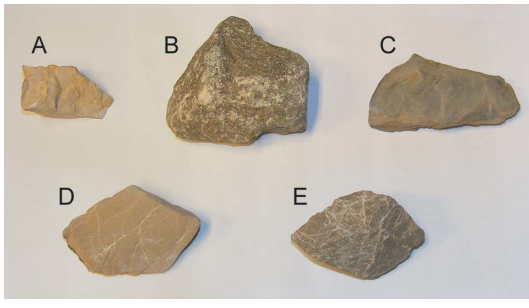

Figure 6
Photographs of the five hand specimens. A: St Louis, Missouri, USA; B: Hope Valley, Peak District, UK; C: Mt Rachais, Grenoble, France; D and E: Mindelheimer Klettersteig, Allgäu Alps, Austro-German border.

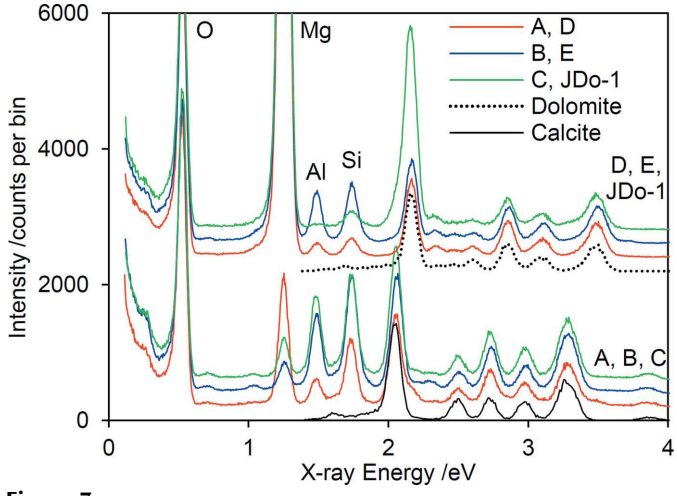

Figure 7
Ca *K* suppressed back-reflection spectra of samples A–E and JDo-1, offset for clarity. Diffraction-only simulations of calcite and dolomite are also shown.

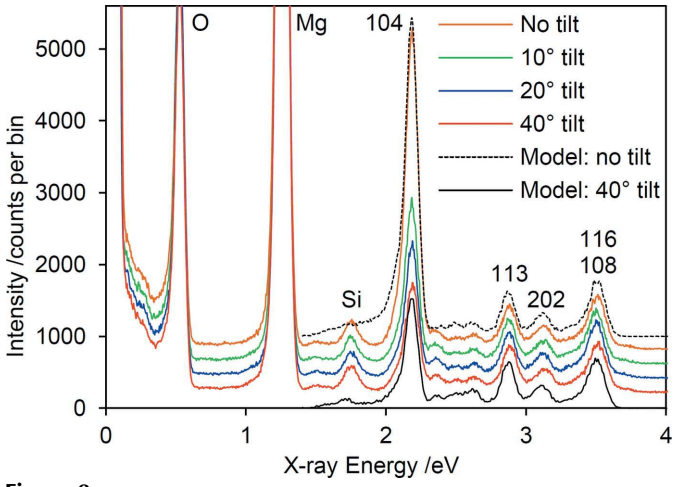

Figure 8
Ca *K* suppressed back-reflection spectra of JDo-1 at several sample tilt angles, and simulations (diffraction-only) including preferred orientation, offset for clarity. Each data set was acquired over two hours. The assignment of the strongest diffraction peaks is shown on the plot. To allow for changes in overall intensity arising from the change in sample position, the experimental data sets with a tilted sample were normalized to the untilted sample data set using the Mg fluorescence peak area. For example, the 40° tilt data set was reduced by 18.4%. The same factor was applied to the simulation for this tilt angle, relative to the simulation for the untilted sample.

6. Discussion and conclusions

The spectra in Fig. 3 clearly show that diffraction peaks obscured by intense fluorescence peaks may be uncovered by tuning the source excitation voltage to just below the corresponding absorption edge. In addition to suppressing the primary fluorescence peaks, the associated escape peaks are also suppressed and the signal-to-background ratio of the diffraction peaks is significantly increased, both of which serve to yield an improved spectrum free from artefacts due solely to the intense primary fluorescence peaks. Elimination of escape peaks potentially reveals additional diffraction or weak fluorescence peaks. The increase in signal-to-background ratios is due to both an increase in the signal (if the X-ray tube emission current can be increased at the lower excitation voltage) and a reduction in the spectrum background. The strength of escape peaks and the background relative to the primary fluorescence peaks depends on the type of solid state detector in use and on other details of the experimental configuration.

The Ca *K* suppressed spectrum of limestone A revealed two diffraction features (Fig. 4) that strongly indicate the presence of dolomite as a secondary mineral. In the spectrum recorded with a higher excitation voltage (Fig. 3), these features are essentially obscured. Dolomite could possibly be identified through increased intensity between the calcite 104 peak at 2.06 keV and the Ca *Kβ* escape peak (and data for limestones B and C, not shown, support this), but the identification and quantification of dolomite based on this feature alone would be much less secure, relying essentially on the inference that dolomite is a probable associated mineral.

The fluorescence suppression method presented here has been shown to work well, in the back-reflection geometry, for limestones and dolomites. Its efficacy for other rock types will depend on the degree of overlap of diffraction and fluorescence peaks and on the number, identities and amounts of the minerals present. For EDXRD in geometries other than back reflection, the diffraction peak energies can be conveniently shifted relative to fluorescence peaks by changing the relative angle of the source and detector, though the suppression of fluorescence by tuning of the source excitation voltage offers an alternative. For back-reflection EDXRD, altering this angle would remove the primary reason for using this geometry in the first place (*i.e.* insensitivity to sample morphology), and fluorescence suppression is therefore an attractive option. Thus, fluorescence suppression is an enabling implementation method for back-reflection EDXRD, overcoming to a large degree the otherwise problematic overlap of fluorescence and diffraction peaks.

The observation of the preferred orientation of crystallites in the pressed-powder pellet of the dolomite reference material JDo-1 illustrates a particular (and perhaps unexpected) advantage of back-reflection EDXRD. Demonstration of preferred orientation was especially straightforward because the method is in other ways insensitive to the sample tilt angle (see Hansford, 2013). These results therefore illustrate a simple method to probe samples, whether unprepared whole rock specimens or not, for preferred orientation. Equally, at least for this limited sample of rocks belonging to the same class, observation of the specimens in their natural states has avoided the preparation-induced preferred orientation of crystallites which otherwise complicates the analysis.

In summary, the results presented in this paper demonstrate the principle of uncovering of diffraction peaks by suppression of fluorescence peaks through tuning of the source excitation voltage below elemental absorption edges. In the analysis of a limestone using the back-reflection geometry, implementation of this method proved crucial to the identification and approximate quantification of a secondary mineral. Fluorescence suppression significantly aids the implementation of back-reflection EDXRD but can also be used in energy-dispersive XRD at other angles. A novel and simple method to observe and quantify the preferred orientation of crystallites, employing the back-reflection technique with sample tilting, was also demonstrated. Five natural unprepared hand specimens of limestones and dolomites showed no preferred orientation.

The authors would like to thank Cheryl Haidon (Geology Department, University of Leicester) for XRD analysis of limestone A with the Bruker D8 Advance, Derek Pullan for provision of limestone A and the referees for suggesting improvements to the paper. This work was supported by grants from the Royal Society and the European Space Agency.

References

Bautz, M. W., Prigozhin, G. Y., Pivovaroff, M. J., Jones, S. E., Kissel, S. E. & Ricker, G. R. (1999). *Nucl. Instrum. Methods Phys. Res. Sect. A*, **436**, 40–52.

Burrows, D. N. (2005). *Space Sci. Rev.* **120**, 165–195.

Caminiti, R. & Albertini, V. R. (1999). *Int. Rev. Phys. Chem.* **18**, 263–299.

Cernik, R. J., Khor, K. H. & Hansson, C. (2008). *J. R. Soc. Interface*, **5**, 477–481.

Černý, R., Valvoda, V. & Chládek, M. (1995). *J. Appl. Cryst.* **28**, 247–253.

Cuevas, A. M. & Gravie, H. P. (2011). *Nucl. Instrum. Methods Phys. Res. Sect. A*, **633**, 72–78.

Dollase, W. A. (1986). *J. Appl. Cryst.* **19**, 267–272.

Ebel, H. (1999). *X-ray Spectrom.* **28**, 255–266.

Ebel, H. (2003). *X-ray Spectrom.* **32**, 46–51.

Ellmer, K., Mientus, R., Weiss, V. & Rossner, H. (2003). *Meas. Sci. Technol.* **14**, 336–345.

Hansford, G. M. (2009). *Rev. Sci. Instrum.* **80**, 073903.

Hansford, G. M. (2011*a*). *J. Appl. Cryst.* **44**, 514–525.

Hansford, G. M. (2011*b*). *Nucl. Instrum. Methods Phys. Res. Sect. A*, **632**, 81–88.

Hansford, G. M. (2012). *Nucl. Instrum. Methods Phys. Res. Sect. A*, **690**, 117–124.

Hansford, G. M. (2013). *Nucl. Instrum. Methods Phys. Res. Sect. A*, **728**, 102–106.

Harding, G. (2009). *Appl. Radiat. Isot.* **67**, 287–295.

Higginbotham, A., Patel, S., Hawreliak, J. A., Ciricosta, O., Collins, G. W., Coppari, F., Eggert, J. H., Suggit, M. J., Tang, H. & Wark, J. S. (2014). *Rev. Sci. Instrum.* **85**, 033906.

Imai, N., Terashima, S., Itoh, S. & Ando, A. (1996). *Geostand. Newsl.* **20**, 165–216.

Kaye, G. W. C. & Laby, T. H. (2005). *Tables of Physical and Chemical Constants*, 16th ed. (1995), ch. 4.2.1, Kaye and Laby Online Version 1.0, http://www.kayelaby.npl.co.uk.

Kellermeier, M., Glaab, F., Klein, R., Melero-García, E., Kunz, W. & García-Ruiz, J. M. (2013). *Nanoscale*, **5**, 7054–7065.

Kirshenbaum, K. C., Bock, D. C., Zhong, Z., Marschilok, A. C., Takeuchi, K. J. & Takeuchi, E. S. (2014). *Phys. Chem. Chem. Phys.* **16**, 9138–9147.

Laine, E. & Lähteenmäki, I. (1980). *J. Mater. Sci.* **15**, 269–277.

Ma, Y., Mao, H., Hemley, R. J., Gramsch, S. A., Shen, G. & Somayazulu, M. (2001). *Rev. Sci. Instrum.* **72**, 1302.

Perdikatsis, V. (2000). *Mater. Sci. Forum*, **321–324**, 128–132.

Peterzol, A., Duvauchelle, P., Kaftandjian, V. & Ponard, P. (2011). *Nucl. Instrum. Methods Phys. Res. Sect. A*, **654**, 450–463.

Potts, P. J. (1992). *A Handbook of Silicate Rock Analysis*, ch. 8. New York: Springer.

Press, W. H., Teukolsky, S. A., Vetterling, W. T. & Flannery, B. P. (2007). *Numerical Recipes*: *The Art of Scientific Computing*, 3rd ed. Cambridge University Press.

Prigozhin, G., Jones, S., Bautz, M., Ricker, G. & Kraft, S. (2000). *Nucl. Instrum. Methods Phys. Res. Sect. A*, **439**, 582–591.

Sánchez del Río, M., Bernstorff, S., Savoia, A. & Cerrina, F. (1992). *Rev. Sci. Instrum.* **63**, 932–935.

Sánchez del Río, M. & Cerrina, F. (1992). *Rev. Sci. Instrum.* **63**, 936–940.

Scarlett, N. V. Y., Madsen, I. C., Evans, J. S. O., Coelho, A. A., McGregor, K., Rowles, M., Lanyon, M. R. & Urban, A. J. (2009). *J. Appl. Cryst.* **42**, 502–512.

Sparks, C. J. Jr & Gedcke, D. A. (1972). *Adv. X-ray Anal.* **15**, 240–253.

Sutton, S. R., Rivers, M. L. & Smith, J. V. (1986). *Anal. Chem.* **58**, 2167–2171.

Suzuki, Y., Morgan, P. E. D. & Niihara, K. (1998). *Powder Diff.* **13**, 216–221.

Uda, M. (2004). *Nucl. Instrum. Methods Phys. Res. Sect. B*, **226**, 75–82.

Uda, M., Ishizaki, A., Satoh, R., Okada, K., Nakajima, Y., Yamashita, D., Ohashi, K., Sakuraba, Y., Shimono, A. & Kojima, D. (2005). *Nucl. Instrum. Methods Phys. Res. Sect. B*, **239**, 77–84.

Voskamp, A. P. (1974). *Adv. X-ray Anal.* **17**, 124–138.